# Pattern formation for $NO+NH_3$ on Pt(100): Two-dimensional numerical results

Hannes Uecker*
*Mathematisches Institut I, Universität Karlsruhe, D-76128 Karlsruhe, Germany*
(Received 30 January 2004; revised manuscript received 24 May 2004; published 11 January 2005)

The Lombardo-Fink-Imbihl model of the $NO+NH_3$ reaction on a Pt(100) surface consists of seven coupled ordinary differential equations (ODE) and shows stable relaxation oscillations with sharp transitions in the relevant temperature range. Here we study numerically the effect of coupling of these oscillators by surface diffusion in two dimensions. We find different types of patterns, in particular phase clusters and standing waves. In models of related surface reactions such clustered solutions are known to exist only under a global coupling through the gas phase. This global coupling is replaced here by relatively fast diffusion of two variables which are kinetically slaved in the ODE. We also compare our simulations with experimental results and discuss some shortcomings of the model.

DOI: 10.1103/PhysRevE.71.016207 PACS number(s): 89.75.Kd, 82.40.Np, 82.20.Wt

## I. INTRODUCTION

Pattern formation on catalytic surfaces has been intensely studied in recent years with most studies focusing on two reaction systems, catalytic CO oxidation and catalytic NO reduction. These reactions have been investigated on various platinum and rhodium single crystal surfaces. A (state-dependent) anisotropy of surface diffusion, global coupling, and adsorbate-controlled surface phase transitions added features to chemical reactions and led to phenomena in pattern formation not known in liquid phase reactions; for general background and reviews see Refs. [1–4].

The catalytic reduction of NO with $NH_3$ to the products $N_2$ and $H_2O$ on a Pt(100) surface has been studied experimentally in Refs. [5,6], including photoemission electron microscopy (PEEM) images showing the spatiotemporal behavior of the reaction. This catalytic surface reaction involves the adsorption of the reactants at the surface, dissociation and reaction on the surface, and desorption of the products from the surface. Additionally, the Pt(100) surface can switch between two substrate configurations, the catalytically active $1\times1$ phase with a bulklike surface termination and a catalytically inert quasihexagonal reconstructed phase ("hex"). The stable state of the clean Pt(100) surface is the hex reconstruction but above a critical adsorbate coverage the $1\times1$ phase is more stable and the reconstruction is lifted. Thus an adsorbate-induced $1\times1\leftrightarrow$hex phase transition is constituted, and for temperatures around 440 K and at low pressure (about $10^{-6}$ mbar) the catalytic conversion process proceeds in a periodic way.

A realistic model for $NO+NH_3$ on Pt(100) has been set up in Ref. [7]. It consists of seven coupled ordinary differential equations (ODE) for the variables $\theta_{NO}^{1\times1}, \theta_{NO}^{hex}, \theta_{1\times1}, \theta_{NH_3}^{1\times1}, \theta_{O}^{1\times1}, \theta_{N}^{1\times1}, \theta_{H}^{1\times1}$, which denote, in that order, the local coverages of NO on the $1\times1$ phase, of NO on the hex phase, the fraction $\theta_{1\times1}$ of the surface in $1\times1$ phase, and the local coverages of $NH_3$, O, N, and H on the $1\times1$ phase. We write the ODE in abstract form as

$$\frac{d}{dt}X = f(X;p,T), \quad X\in\mathbb{R}^7, \quad f=(f_1,\ldots,f_7), \tag{1}$$

where $p\in\mathbb{R}^{11}$ is a vector of temperature independent parameters. Moreover, (1) contains 11 rate constants depending by the Arrhenius law on temperature $T$, which we therefore display explicitly. In $p$ there are two external (tunable) parameters, $p_{NO}$, and $p_{NH_3}$, acting as driving forces and corresponding to a constant supply of NO and $NH_3$, respectively, from the gas phase.

The ODE (1) has periodic solutions in a parameter range similar to the experiment. However, the oscillations in (1) are more anharmonic than in the experiment. In Sec. II A we plot typical periodic orbits of (1), but we will not repeat in detail the properties of this ODE; see the Appendix for the equations, and Refs. [7,8] for discussion and numerical analysis of (1). Here we consider linear coupling of these ODE oscillators by surface diffusion in two-dimensions (2D), i.e., we study the reaction-diffusion system

$$\frac{d}{dt}X(t,\vec{x}) = f(X(t,\vec{x});p,T) + M(T)\Delta X(t,\vec{x}), \tag{2}$$

where $M(T)$ is the diagonal diffusion matrix depending by the Arrhenius law on $T$ and the diffusion energies $\vec{E}$. Depending on the parameters we find a rich variety of spatiotemporal patterns by direct numerical integration of (2). Our work then has the following two goals: (a) to present examples of the interesting patterns for (2) and thus give a motivation and some starting points for the analysis of (2) from an abstract pattern formation point of view, and (b) to assess the quality of model (2) and to identify realistic parameters for the diffusion energies in (2) by comparison with PEEM images and further data from experiment [5,6].

The diffusion energies $\vec{E}$ are not external parameters in the experiment. Nevertheless we focus on the dependence of (2) on $\vec{E}$, i.e., we change $M(T)$ independent of $T$, since $\vec{E}$ is known only rather roughly from experiment or first principles. We also study the temperature dependence of (2) which shows a shortcoming of the model and suggests that a global coupling should be introduced (see later). The remain-

*Electronic address: hannes.uecker@math.uni-karlsruhe.de

 

ing (ODE) parameters, in particular the partial pressures $p_{NO}$ and $p_{NH_3}$, are kept fixed.

The model (2) has been studied in one dimension (1D) in Ref. [9]. There the patterns were classified into four groups (see Sec. II D for illustration): bulk oscillations (BO), phase clusters (PC), standing waves (SW), and phase waves (PW). Even in 1D a systematic study of the dependence of the patterns on the parameters and the initial conditions is hard. In 2D, additional geometric effects play an important role and for SW and PC lead to metastable patterns and very long transients. Of course, numerics also become *a priori* much more expensive in 2D [1].

Bulk oscillations means that the whole surface oscillates homogeneously in the limit cycle of (1), while in both PC and SW the oscillations are organized into macroscopic areas (clusters) in such a way that the phase changes from one area to the next in a regular way, with phase shifts of half a period. The difference between PC and SW is that in SW the phase pattern has an intrinsic spatial wave length, while in PC the clusters have no intrinsic size and grow until the whole domain is split into only two clusters. Here we follow [10–13] in the terminology, but also loosely term both SW and PC as clustering. The clustering requires substantial deviations from the periodic ODE orbits at the cluster boundaries. In contrast, PW means that the phase changes smoothly and each oscillator is always close to the periodic ODE orbit.

The transitions between the different regimes are rather delicate. The system is most sensitive with respect to the (relatively slow) NO diffusion on the $1\times1$ and the hex phase. This agrees well with the analysis in Ref. [8] where it is shown that $\theta_{NO}^{1\times1}$, $\theta_{NO}^{hex}$, and $\theta_{1\times1}$ are the "master" dynamic variables for (1) (in the oscillatory regime) while the remaining four are "slaved." However, $\theta_{1\times1}$ does not diffuse, which gives NO diffusion its special importance.

Of course, BO, PC, SW, and PW (and the competition between these patterns) are also interesting from a theoretical point of view. Phase waves for oscillators close to a Hopf point can be analyzed using phase diffusion equations; see, e.g., Refs. [14–16]. However, relaxation oscillators may behave quite differently under (weak) coupling than harmonic oscillators [17–19]; in particular, under certain conditions phase waves cease to exist; see Ref. [9] for discussion and further references. On the other hand, SW can be generated in simple reaction-diffusion systems via the so called wave bifurcation [20–22]. This, however, again corresponds to a (roughly) harmonic time (and space) dependence.

In surface catalysis, clustering has been intensively studied for the CO oxidation on Pt(110), both experimentally and theoretically [10–13,23–26]. Here the reaction-diffusion models have considerably simpler ODE dynamics than (1) (three dimensional or, in a refined version, four dimensional), but additional to the surface diffusion there is a *global* coupling through the gas phase in the spatially extended system. Moreover, external forcing [13] and/or global delayed feedback [11,23,24,27] have been used to *control* the pattern formation in this system. In Ref. [28] a condensed model of surface catalysis with long range coupling has been studied by direct numerical simulation and an extremely rich variety of cluster patterns has been obtained. See also Refs. [29–31] for experimental results on clustering in the Belousov-Zhabotinsky with global feedback and a model of this problem with two dimensional kinetics.

The ODE (1) can also be reduced to a three dimensional system

$$\frac{\mathrm{d}}{\mathrm{d}t}y = g(y;p,T), \quad y = \begin{pmatrix} \theta_{NO}^{1\times1} \\ \theta_{NO}^{hex} \\ \theta_{1\times1} \end{pmatrix}, \tag{3}$$

$$g(y) = \begin{pmatrix} f_1[\theta_{NO}^{1\times1}, \theta_{NO}^{hex}, \theta_{1\times1}, h(y)] \\ f_2[\theta_{NO}^{1\times1}, \theta_{NO}^{hex}, \theta_{1\times1}, h(y)] \\ f_3[\theta_{NO}^{1\times1}, \theta_{NO}^{hex}, \theta_{1\times1}, h(y)] \end{pmatrix},$$

for the slow variables $y$ by elimination of the fast variables $z=(\theta_{NH_3}^{1\times1}, \theta_{O}^{1\times1}, \theta_{N}^{1\times1}, \theta_{H}^{1\times1})$ [8]. The reduction of dimension in (3) is of course advantageous both analytically and numerically. Naively, we may then study the reaction diffusion problem

$$\frac{\mathrm{d}}{\mathrm{d}t}y = g(y;p,T) + M_{red}\Delta y \tag{4}$$

with $M_{red}=\mathrm{diag}(D_{NO}^{1\times1}, D_{NO}^{hex}, 0)$. However, as already discussed in Ref. [9], although the error between (1) and (3) is small, obviously all the influence of the (relatively fast) diffusion of $NH_3$ and H is lost in going from (2)–(4). On the other hand, the elimination of kinetically slaved variables from PDE like (2) can be done analytically only in special cases, see, e.g., Ref. [32], and numerically yields little advantage.

Note that (4) corresponds to (2) in the limit $D_{NH_3}$, $D_H=0$. We find that no clustering occurs in this limit or even for relatively slow diffusion of $NH_3$ and H. This has two consequences:

(1) it means that to study the model for realistic values of $M(T)$ we must simulate the full system (2);[2] and

(2) more importantly, it shows that, additional to the relaxation type of the oscillations, a *key ingredient* for clustering in (2) is a *nonlocal* (or long range) coupling due to relatively fast diffusion of the kinetically slaved variables $\theta_{NH_3}^{1\times1}$ and $\theta_{H}^{1\times1}$.

The most important difference between 1D and 2D are curvature effects. One result is that the (nontrivial) clustered solutions presented here do not become strictly periodic during simulation time. Instead, these solutions become *nearly periodic*: this means that the antiphase oscillations of well

[1] A typical simulation of 4000 s of simulated system time on $128\times128$ grid points runs about 100 h on a 2.4 GHz Pentium 4 machine with 512 MB RAM and similar machines, see Sec. II C.

[2] The kinetically slaved and immobile variables $\theta_{O}^{1\times1}$ and $\theta_{N}^{1\times1}$ can be eliminated from (2) as long as the solution is sufficiently close to the periodic ODE orbit at each point in space, which is more and more violated the more complicated the solutions become. In any case, the speedup is small.

defined clusters can be observed over many (ODE) periods, but the boundaries or nodal lines between the clusters slowly drift. There are also solutions for (2) in which SW in annular shape initially develop. These look similar to target patterns. However, they are unstable and depending on geometric constraints like the domain size, they either relax to quasi-1D SW in a long transient process or evolve into irregular SW. In contrast, in 1D in the same parameter regimes all solutions are quite regular and eventually become periodic, which may include periodic changes of the cluster boundaries (oscillating phase clusters).

An important effect of the clustering is that it reduces the periods of oscillations of macroscopic (i.e., spatially averaged) quantities by a factor of (roughly) 2. Moreover, while (1) has relaxation oscillations with sharp transitions, the averaged quantities oscillate more harmonically. Both effects together yield a better agreement of averaged quantities for the model with experimental data ([7], Figs. 7 and 3). However, the *spatio*temporal agreement of (2) with the experimental results [6] is not satisfying. By properly adjusting the relative magnitude of the diffusion constants within chemically realistic ranges we do get patterns (standing waves) on comparable spatial scales, but the temperature dependence of the model does not match the experimental data (see below). Moreover, in Ref. [6] the observed patterns have been explained in terms of front dynamics, while in the model SW and PC dominate for realistic values of the diffusion constants. As noted, mathematically one should make a clear distinction between phase dynamics (fronts) where every oscillator is always close to the ODE limit cycle, and clustered patterns where this is not true at the cluster boundaries. In Sec. III F we shall argue that in fact the distinction is more gradual in the model (2). In particular, there are still local front dynamics within "clusters of equal phase." These local fronts then reproduce qualitatively the front dynamics seen in the PEEM images [6], though the front speed is too fast (roughly by a factor of 10) in our simulations.

The most serious shortcoming of the model is a reversed temperature dependence of the spatial pattern size. In a nutshell, increasing $T$ in (2) decreases the spatial scale of the patterns, while in the experiment it is the other way round. We note again that there is *no global gas-phase coupling* in (2), although it most likely plays an important role in the experiment. In particular, bulk oscillations at high $T$ and the gradual failure of long range synchronization at lower $T$ in the experiment are attributed to the global gas-phase coupling at high $T$ and its breakdown at lower $T$ [33]. It remains to be seen if the inclusion of such a global coupling into (2) will improve the temperature dependence of the model.

The remainder of this work is organized as follows. The preparatory Sec. II contains remarks on the periodic orbits for (1), the diffusion constants, the numerical method, and the choice of initial conditions and domain size for (2). In Sec. III we present our results. Conclusions are summarized in Sec. IV, while the Appendix contains the ODE (1). Movies and additional simulations are available via internet [34].

## II. THE SETUP

### A. The periodic ODE orbits

Figure 1 shows periodic orbits $\gamma(T)$ for (1) at $T=410,420,430$ K. The partial pressures are $p_{NO}=1.1\times10^{-6}$ mbar and $p_{NH_3}=4.7\times10^{-6}$ mbar, as in Ref. [7]. In (a) we present all seven dynamic variables, while (b) shows the chemically interesting production rates $r_{N_2}=0.5N_s k_9(\theta_N^{1\times1})^2/\theta_{1\times1}$ of $N_2$ and $r_{H_2O}=N_s k_8\theta_O^{1\times1}\theta_H^{1\times1}/\theta_{1\times1}$ of $H_2O$, where $N_s=1.3\times10^{15}$ cm$^{-2}$ is the concentration of surface sites. The most important conclusions from Refs. [7,8] are as follows. One period is divided into four segments. We plot $\theta_{1\times1}$ first since the decay of $\theta_{1\times1}$ in segment 1 sets the slowest time scale in the largest segment; here all other variables follow $\theta_{1\times1}$ adiabatically. This breaks down in segment 2, where adsorbtion of NO starts the hex$\rightarrow1\times1$ phase transformation in segment 3. In segment 4 the so called, "surface explosion" occurs with a rapid production of $N_2$ and $H_2O$. The $NH_{x,ad}/H_{ad}$ layer built up this way is unable to stabilize the $1\times1$ phase, and the process repeats with the slow relaxation to the hex phase in segment 1.

The temperature dependence is illustrated in (c). For lower $T$ the (average) fraction $\theta_{1\times1}$ of the $1\times1$ phase increases, while the amplitude of the oscillations and the reaction rates decrease, and vice versa for higher $T$. The period $t_0$ also depends on $T$ but only slightly in the middle of the oscillatory regime considered here. We have $t_0(420\text{ K})\approx97$ s. Below the lower threshold ($T\approx404$ K) for oscillations the surface is completely in the $1\times1$ phase ($\theta_{1\times1}=1$), while above the upper threshold ($T\approx433$ K) it is in the hex phase ($\theta_{1\times1}=0$). In both cases, the production rates $r_{N_2}$ and $r_{H_2O}$ are zero. For the reaction diffusion problem (2) two observations from Fig. 1 are most important: the smaller (larger) amplitudes at lower (higher) temperatures yield smaller (larger) spatial gradients for oscillators with shifted phases, and the transitions become less (more) sharp for lower (higher) $T$; see Ref. [9] and Sec. III D.

### B. The diffusion constants

Surface diffusion constants are difficult to measure [35]. For the diffusion constants for Pt(100)/H,N,O,NO,$NH_3$ we follow the arguments given in Ref. [9], based on Ref. [35,36]. In the temperature range considered here, O and N are considered immobile. As usual, we approximate the remaining $D_i$ using the Arrhenius-law $D_i=\nu e^{-\tilde{E}_i/RT}$, where $R=8.3144$ J K$^{-1}$ mol is the universal gas constant, $\nu=0.001$ cm$^2$ s$^{-1}$ is a common prefactor, and $\tilde{E}_i$ is the activation energy for diffusion of the respective species. This yields the data in Table I, which, however, should be seen as rough estimate only, hence, as a starting point for the numerical simulations.

The diffusion constants differ quite significantly in magnitude: diffusion of $NO_{1\times1}$ and $NO_{hex}$ is relatively slow and that of H and $NH_3$ relatively fast. In this sense (strictly speaking for $D_{NO}^{1\times1}=D_{NO}^{hex}=0$) (2) is related to the model problem in Ref. [37] where a field of oscillators is coupled by diffusion through a passive medium. In Sec. III we find that the "typical pattern size" $l_p$ for (2) at $T=420$ K is of the order of 0.01 cm. Hence $\sqrt{D_{NH_3}\tau}\approx2.4\times10^{-3}$ cm and $\sqrt{D_H\tau}\approx1.8\times10^{-3}$ cm, where $\tau=1$ s is our time scale, are roughly of the magnitude as $l_p$ and diffusions of $\theta_{NO}^{hex}$ and $\theta_N^{1\times1}$ introduce a nonlocal but also nonglobal coupling, where

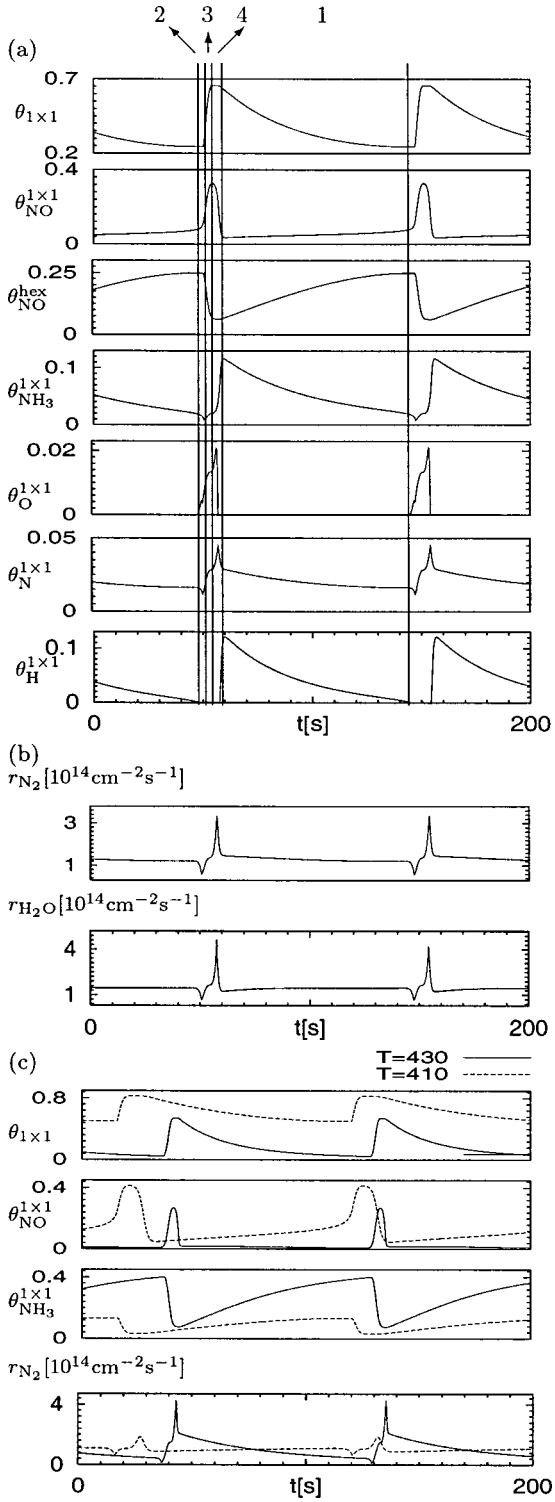


FIG. 1. (a) periodic ODE orbits at $T=420$ K, (b) production rates at $T=420$ K, (c) $\theta_{NO}^{1\times1}$, $\theta_{NO}^{hex}$, $\theta_{1\times1}$, $r_{N_2}$ at $T=410$, 430 K; time in s, the fraction $\theta_{1\times1}$ of the surface in the $1\times1$ state is dimensionless, coverages in ML=monolayers=(number of adsorbed molecules)/(number of free sites on the surface). Quantities from these ODE orbits will henceforth be referred to as, e.g., $\theta_{1\times1}^{ODE}$, and the unit for coverages (ML) will be omitted for convenience.

TABLE I. Diffusion energies and constants. For convenience we write $\vec{E}=(\widetilde{E}_{NO}^{1\times1},\widetilde{E}_{NO}^{hex},\widetilde{E}_{NH_3},\widetilde{E}_{H})$. NA means not applicable.

| Process | Parameter | $\widetilde{E}$ (kJ mol$^{-1}$) | Value at 420 K (cm$^2$ s$^{-1}$) |
|---|---|---|---|
| NO diffusion $(1\times1)$ | $D_1=D_{NO}^{1\times1}$ | 28 | $3.3\times10^{-7}$ |
| NO diffusion (hex) | $D_2=D_{NO}^{hex}$ | 24 | $1\times10^{-6}$ |
| NA | $D_3=0$ | NA | Always=0 |
| $NH_3$ diffusion | $D_4=D_{NH_3}$ | 15 | $1.4\times10^{-5}$ |
| O diffusion | $D_5=D_O$ | | Set to 0 |
| N diffusion | $D_6=D_N$ | | Set to 0 |
| H diffusion | $D_7=D_H$ | 18 | $5.7\times10^{-6}$ |

local (global) coupling would correspond to $\sqrt{D_{NH_3}}\tau \ll l_p(\sqrt{D_{NH_3}}\tau \gg l_p)$.

### C. Numerical method and choice of initial conditions and system size

To discretize (2) we choose a system size $L$, and consider $n\times n$ oscillators $X(\cdot,i,j)=X(\cdot,x_i,y_j)$ at $(x_i,y_j)=(i\delta,j\delta)$, $i,j=1,\ldots,n$, $\delta=L/(n-1)$, with periodic boundary conditions. The numerical scheme is the same as in Ref. [9]: a split-step method, where the ODE part is integrated using the linearly implicit solver limex ([38], Sec. 6.4) (available online at www.zib.de/SciSoft/CodeLib/ivpode.en.html) and the linear PDE-part $(d/dt)X=M\Delta X$ using an implicit Fourier spectral method. In our simulations we use $\delta=0.0005$ cm and the average effective time steps are about $dt=0.001-0.01$ s (depending on the parameters). Convergence in $\delta$ was checked by reducing $\delta$ by a factor of 2 and comparison.

The initial conditions for (2) were chosen as localized perturbations of the point

$$Z_0=(0.03,0.24,0.22,0.5\times10^{-6},0.01,0.02,0.22)$$

which is roughly near the end of segment 1 of the periodic orbit $\gamma(420)$, cf. Fig. 1. That means, we first assign $X|_{t=0}(i,j)=Z_0$ to all oscillators, then choose $l\in\{0,\ldots,7\}$ and $a\in\mathbb{R}$, and add a perturbation of amplitude $a$ to the $l$th component in part of the domain. In formulas, we set

$$X_l|_{t=0}(i,j)=\begin{cases} z_l+a, & (i,j)\in\mathcal{I},\\ z_l & \text{elsewhere,}\end{cases} \tag{5}$$

where $\mathcal{I}\subset\mathbb{N}^2$ is an index set. For some $k<n$ we set $\mathcal{I}=\mathcal{I}_k=\{(i,j):0\leq i,j\leq k\}$, i.e., we perturb in a square in the upper left. The BO solution $X_{BO}$ is asymptotically stable in the parameter regime given by Table I. Hence, in (5) we need sufficiently large $k$ and/or $a$, depending on $l$, to push the system at least transiently away from $X_{BO}$. As should be expected from the ODE reduction (3), the easiest way to perturb the system away from $X_{BO}$ is to introduce perturbations in $\theta_{NO}^{1\times1}$, $\theta_{NO}^{hex}$ or $\theta_{1\times1}$, i.e., to choose $l\in\{1,2,3\}$. For the sake of brevity we restrict to perturbations in $\theta_{1\times1}$ ($l=3$). Note that this way we add a perturbation to a nondiffusive component and, hence, the system can only be driven back to

or further away from $X_{\mathrm{BO}}$ by coupling to the diffusive components.

We also use random initial conditions in the form

$$X_l|_{t=0}(i,j) = r_{i,j,l} z_l, \tag{6}$$

where each $r_{i,j,l}$ is a (pseudo)random number between 0.5 and 1.5. Choosing a new $r_{i,j,l}$ for each $(i,j)$ tends to yield BO. Hence, the initial data was *preclustered* by choosing the same $r_{i,j,l}$ on squares of certain side lengths $q$.

The experimental data in Ref. [6] was reported for a sampled area of about 1 $\mathrm{mm}^2$, while the PEEM images show circular areas of about 0.5 mm diameter. Here we use $n=128$ in most simulations, hence, $L=(n-1)\delta=0.635$ mm, which is comparable to the size of the PEEM images. We also show some simulations with $n=64$ and one with $n=256$ to illustrate the influence of the system size which unlike in the 1D case plays an important role in 2D. Besides faster computation the advantage of smaller domains lies in shorter transient behavior. However, this may also introduce artificial constraints, see Sec. III E. Using $n=128$ is a good choice to obtain meaningful results in acceptable computation time.

We focus on plotting $\theta_{1\times1}(t,x,y)$ as the main diagnostic for (2). As explained in Sec. II A, the decay of $\theta_{1\times1}$ sets the timescale in the largest segment 1 of the ODE-orbits. Hence, for the reaction-diffusion problem we expect that for given $\theta_{1\times1}$ the remaining variables can roughly be read from Fig. 1, at least at values in segment 1 of the ODE orbit. This turns out to be true [9]. To visualize the spatiotemporal patterns we use 2D plots of $\theta_{1\times1}$ at fixed time, and space-time plots of $\theta_{1\times1}$ along a diagonal through the 2D domain. These plots are further complemented with diagnostics like local time series and the spatial average $\langle\theta_{1\times1}\rangle(t) = (1/n^2)\Sigma_{i,j=1}^{n}\theta_{1\times1}(t,i,j)$.

### D. Classification in 1D

In Fig. 2 we show greyscale plots from Ref. [9] illustrating BO, PC, SW and PW in 1D, $\delta=0.005$ mm, $n=80$, hence, spatial size $L=0.395$ mm, where the initial conditions are the 1D analog of (5). The solutions in (a),(c), and (d) become perfectly periodic after a rather short time transient. The PC solution in (b) shows oscillations of the cluster boundaries. However, these oscillations are much smaller than in 2D; see later.

## III. SIMULATIONS

We first present examples of different patterns at $T=420$ K and $L=0.635$ mm. Temperature dependence and dependence on system size are discussed in Secs. III D and III E later. We also start with a clear distinction between clustered solutions (PC and SW) and phase dynamics (PW), while local phase dynamics within clustered solutions are discussed in Sec. III F. Finally, the patterns will be compared with experimental results in Sec. IV.

The BO solution is asymptotically stable near the parameter regime given in Table I. Therefore we directly start with a more interesting solution.

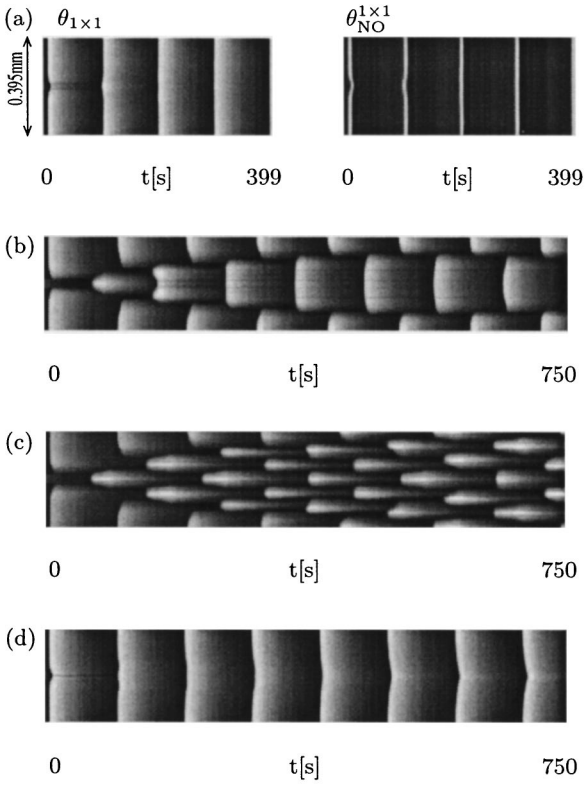


FIG. 2. Examples from Ref. [9] for BO, PC, SW, and PW in 1D. $T=420$ K, greyscale plots of $\theta_{1\times1}(t,x)$ [and $\theta_{\mathrm{NO}}^{1\times1}(t,x)$ in (a)], horizontal axis $t$, vertical axis $x$, spatial size $L=0.395$ mm. The parameters are $\vec{E}=(28,24,15,18)\mathrm{kJ\,mol}^{-1}$ in (a),(b); $\vec{E}=(30,22,15,18)\mathrm{kJ\,mol}^{-1}$ in (c), $\vec{E}=(28,22,25,25)\mathrm{kJ\,mol}^{-1}$ in (d). (a) Stable BO: small initial perturbation is quickly repaired. (b) PC: larger initial perturbation yields phase clusters that split the domain into two halfs. (c) SW: clustering with intrinsic spatial length. (d) PW: smooth phase changes. In (b)–(d), as in the figures to follow, in order to avoid overcrowded pictures we do not repeat the spatial size $L$ in the plots if it is the same as in the previous frame. Similarly, all greyscale plots show $\theta_{1\times1}$ unless noted otherwise.

### A. Phase clusters

In our first simulation we use $T=420$ K, the diffusion data from Table I, $n=128$, hence, $L=0.635$ mm, and initial conditions according to (5) with $k=16$ and $a=0.1$. This yields a 2D PC solution. Figure 3(a) shows snapshots of $\theta_{1\times1}(t,\cdot)$ for the initial evolution. The greyscales are linear interpolations between $z_{\min}=\mathrm{black}=0.2$ and $z_{\max}=\mathrm{white}=0.8$; in the following this is denoted by $z_{\mathrm{scal}}=z_{\min},z_{\max}$.

The larger value of $\theta_{1\times1}$ at $t=0$ s in the top left corner dilutes the NO adsorption in the $1\times1$ phase; in this way we inhibit the hex$\rightarrow1\times1$ phase transition in this part of the surface, which in the remaining part takes places around $t\approx7$ s. Then at $t\approx62$ s, $\theta_{1\times1}$ has sufficiently decayed in the top left corner for the hex$\rightarrow1\times1$ phase transition to start, while in the remainder of the domain $\theta_{1\times1}$ is still decaying along segment 1 of the ODE orbit. For larger $t$ this develops into a PC solution: cluster 1 roughly sits in the top left corner of the domain while cluster 2 fills the rest of the domain. Near $t=750$ s both clusters have about the same area. This

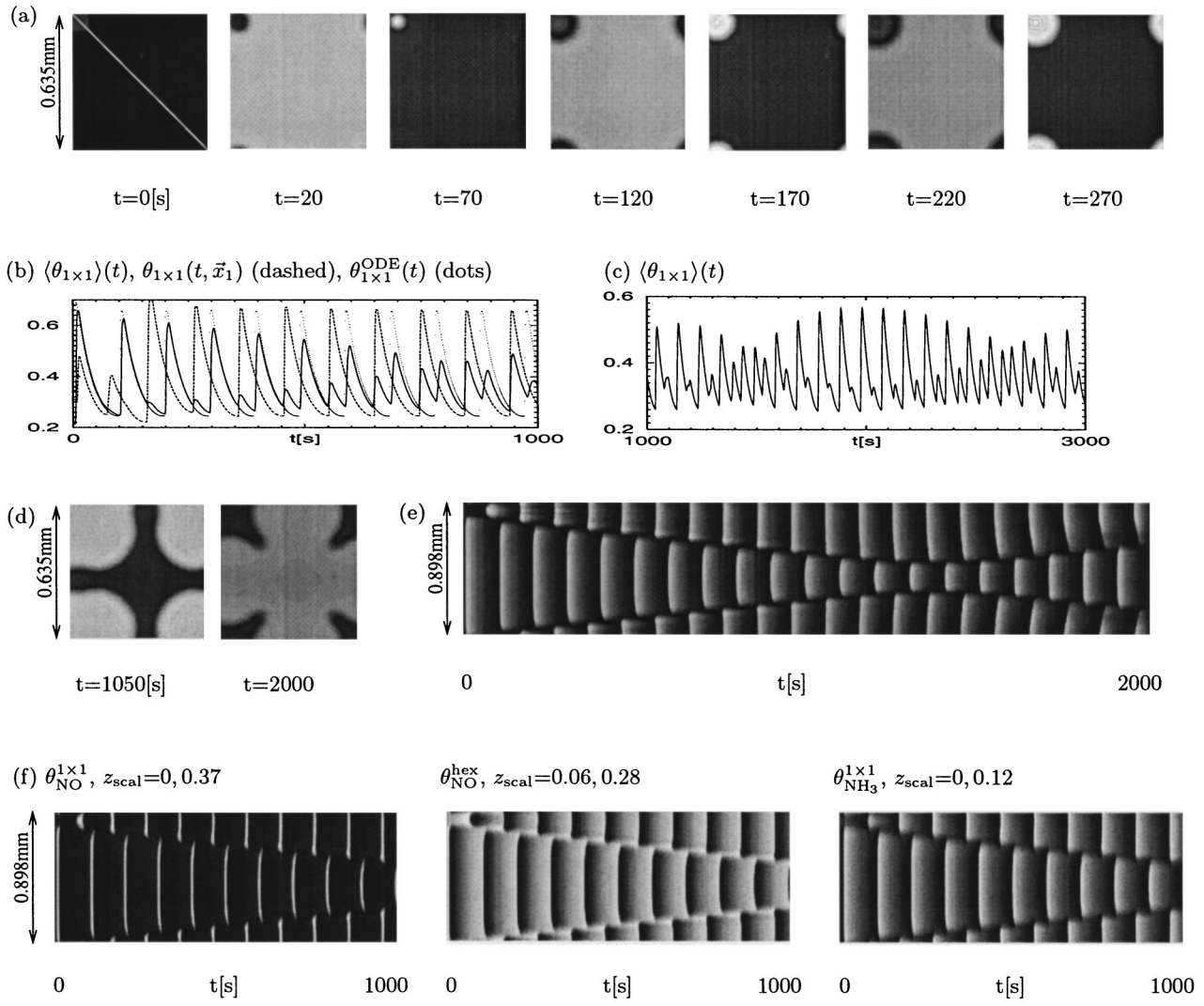


FIG. 3. Phase clusters: $T=420$ K, domain size $L\times L$ with $L=0.635$ mm ($n=128$), $\vec{E}=(28,24,15,18)$kJ mol$^{-1}$, initial data according to (5) with $a=0.1$, $k=16$. (a),(d) $\theta_{1\times1}(t,\cdot)$. (e), (f) space-time plots along the diagonal (length $\sqrt{2}L$) marked in the first frame of (a). The point $\vec{x}_1$ for the local time series in (b) is the top left corner. $z_{\mathrm{scal}}=0.2$, 0.8 in (a), (d), and (e).

can be seen from the full line in (b) showing the spatial average $\langle\theta_{1\times1}\rangle(t)$. Here we also plot the local time series $\theta_{1\times1}(t,\vec{x}_1)$ of the point in the top left corner and $\theta_{1\times1}$ from the ODE solution. These two curves suggest that at $\vec{x}_1$ the solution is close to the ODE limit cycle. This can be checked by closer inspection of the solutions and is true for all points in the interior of a cluster; see also (f).

Unlike the 1D case, the areas of the two clusters do not become almost equal and constant in time. Instead, the boundary between the two clusters oscillates as illustrated in (c). In 1D, such oscillations of the cluster size are much smaller in amplitude and almost negligible for the present parameters. Hence, these oscillations must be attributed to curvature effects in 2D. Previewing Sec. III E we remark that the oscillations become smaller on smaller domains. However, also on smaller domains there is in general no phase balancing, i.e., the areas of antiphase clusters do not become equal. In (d) we show snapshots of $\theta_{1\times1}$ at times where clusters 1 and 2 have become maximal in area, respectively. Panel (e) shows a space-time plot of $\theta_{1\times1}$ along the diagonal marked in (a), while (f) shows three of the remaining components. This illustrates that except at the nodal line between the clusters the solution is always close to the ODE orbit, and how the clustering looks in these components.

Initial conditions according to (5) have the advantage of being well controlled, but they are also artificial. In Fig. 4 we use the same parameters as before but now with random initial data according to (6). Locally the initial data is quickly smoothed out as can be seen from the first two frames in (a). At $t=100$ s the solution shows a number of clusters. The further evolution first shows a coarsening process.

At $t=1000$ s the domain is split into only two clusters of almost equal area. This configuration is remarkably stable: in the further evolution there is only a slow drift of the cluster boundaries, i.e., this solution is *nearly periodic*, which can also be seen from $\langle\theta_{1\times1}\rangle$ in (b). Similarly, the space time plot in (c) also indicates the rather slow adjustment of the cluster boundaries already between $t=500$ s and $t=1000$ s, though it

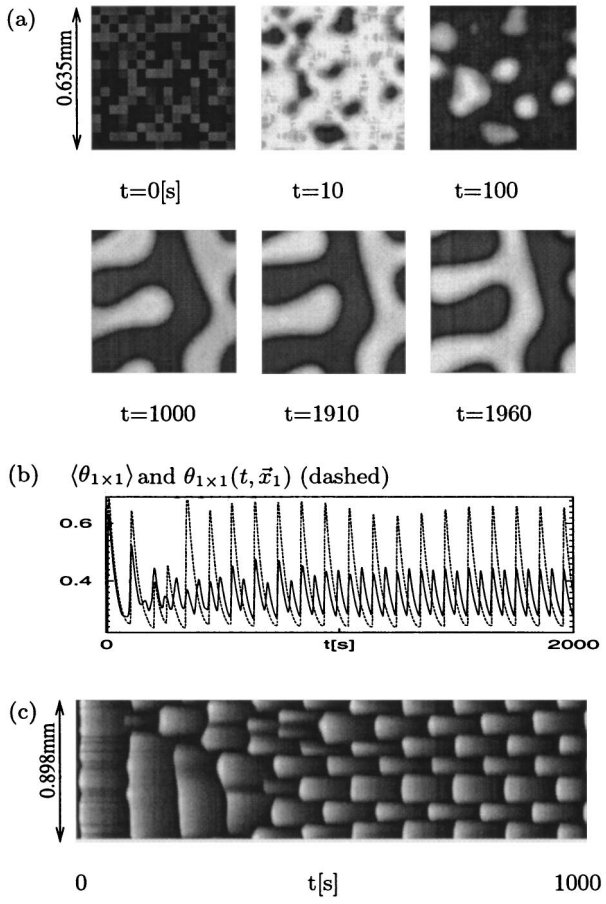


FIG. 4. Phase clusters for random initial data: $T=420$ K, $L=0.635$ mm, $\vec{E}=(28,24,15,18)$kJ mol$^{-1}$, initial data according to (6) with $q=8$. (a) snapshots of $\theta_{1\times1}(t,\cdot)$. (c) $\theta_{1\times1}$ diagonal space-time plot. $z_{\mathrm{scal}}=0.2$, 0.8 in all greyscale plots.

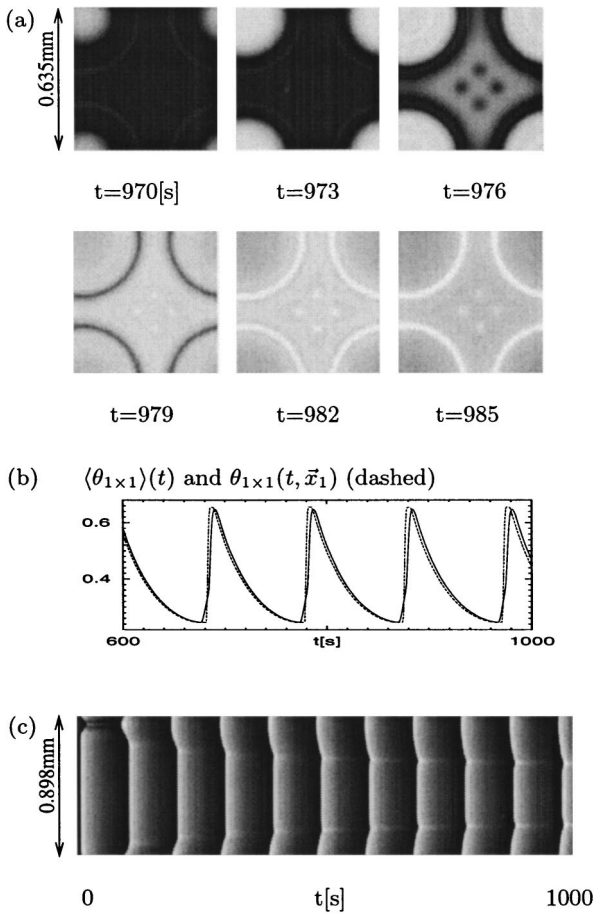


FIG. 5. Phase dynamics for slower diffusion of $\theta_{\mathrm{NH_3}}^{1\times1}$, $\theta_{\mathrm{N}}^{1\times1}$: $T=420$ K, $\vec{E}=(28,24,30,30)$kJ mol$^{-1}$, $L=0.635$ mm, initial data as in Fig. 3. (a) $\theta_{1\times1}(t,\cdot)$. (c) $\theta_{1\times1}$, diagonal space-time plot. $z_{\mathrm{scal}}=0.2,0.8$ in all greyscale plots.

of course fails to capture the geometry of the solution.

### B. Phase waves

Figure 5 gives an example of a PW. We again use $T=420$ K and the same initial data as in Fig. 3 but now $\vec{E}=(28,24,30,30)$kJ mol$^{-1}$. Hence, diffusion of $\theta_{\mathrm{NH_3}}^{1\times1}$ and $\theta_{\mathrm{N}}^{1\times1}$ is now slower than that of $\theta_{\mathrm{NO}}^{1\times1}$ and $\theta_{\mathrm{NO}}^{\mathrm{hex}}$. At $t\approx970$ s in (a), $\theta_{1\times1}$ has started to grow in the top left corner. This triggers a circular front which starts to spread. Near $t\approx976$ s, $\theta_{1\times1}$ also increases in the middle of the domain. The front then collides with this structure. Subsequently $\theta_{1\times1}$ decreases along segment 1 of the ODE orbit with a small phase gradient throughout the domain. This can be clearly seen in the diagonal space-time plot in (c). For larger $t$ the profile along the diagonal roughly keeps its shape. The time series in (b) shows that $\langle\theta_{1\times1}\rangle$ is slightly smeared out by the PW compared to the sharp transitions in $\theta_{1\times1}^{\mathrm{ODE}}$.

On larger domains we can also produce longer fronts which further smear out the transitions in $\langle\theta_{1\times1}\rangle$ (see Ref. [9] for 1D examples). In PW, every oscillator is always quite close to the periodic ODE orbit $\gamma(T=420\ \mathrm{K})$, with some small deviations only during the collisions of the fronts. Hence, in contrast to clustered solutions this situation should be describable by pure phase models ([14] Sec. IV).

Similar front dynamics are always obtained for large values of $\tilde{E}_{\mathrm{NH_3}}$ and $\tilde{E}_{\mathrm{H}}$ (small values of $D_{\mathrm{NH_3}}$ and $D_{\mathrm{H}}$). We conclude that it is the nonlocal coupling by fast diffusion of $\theta_{\mathrm{NH_3}}^{1\times1}$ and $\theta_{\mathrm{N}}^{1\times1}$ that prevents, for instance, the solution at $t=70$ s in Fig. 3(a) to trigger a similar front. Hence the fast diffusion of $\theta_{\mathrm{NH_3}}^{1\times1}$ and $\theta_{\mathrm{N}}^{1\times1}$ is *one key ingredient for the clustering*.

### C. Standing waves

In Ref. [9] it was found that in 1D (in the clustering regime, i.e., for large $D_{\mathrm{NH_3}}$, $D_{\mathrm{H}}$) the diffusions of $\theta_{\mathrm{NO}}^{1\times1}$ and $\theta_{\mathrm{NO}}^{\mathrm{hex}}$ play the following roles: decreasing (increasing) $D_{\mathrm{NO}}^{1\times1}$ ($\tilde{E}_{\mathrm{NO}}^{1\times1}$) may switch the system from PC (clustering with no intrinsic length scale) to SW (clustering with intrinsic length scale) and for SW decreases the spatial size of the clusters. Decreasing (increasing) $D_{\mathrm{NO}}^{\mathrm{hex}}$ ($\tilde{E}_{\mathrm{NO}}^{\mathrm{hex}}$) acts the other way round. See also Figs. 2(b) and 2(c) for illustration in 1D. We now illustrate the similar effect in 2D.

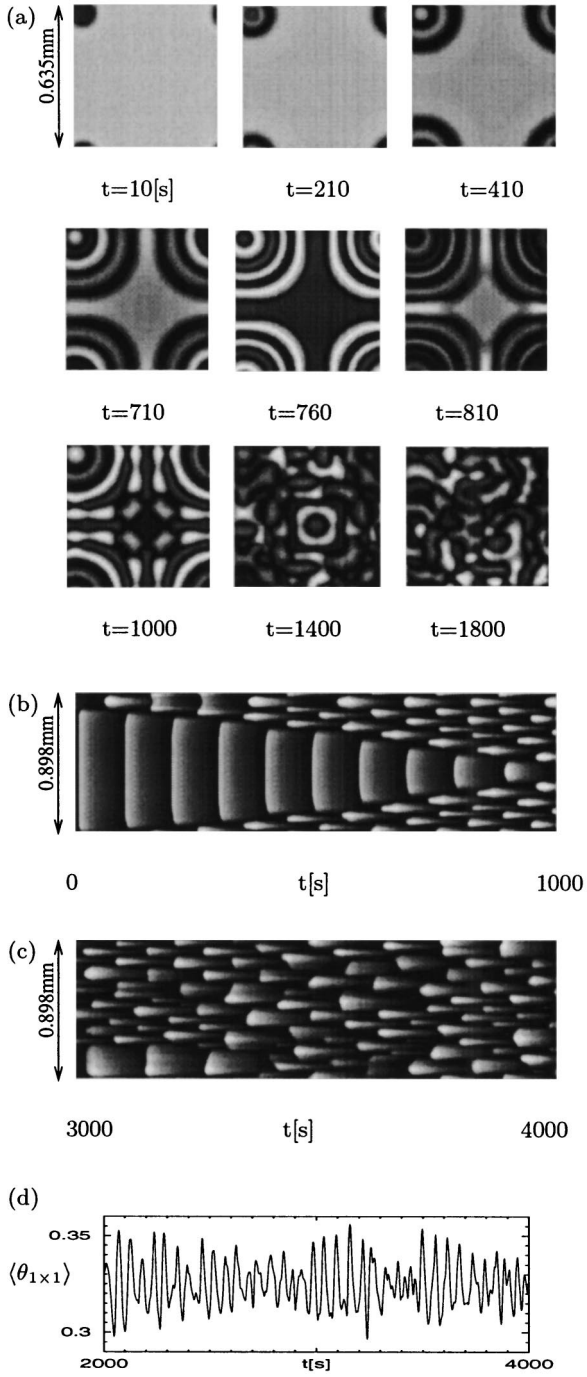


FIG. 6. Irregular standing waves: $T=420$ K, $\vec{E}=(30,22,15,18)$kJ mol$^{-1}$, $L=0.635$ mm, initial data as in Fig. 3. (a) $\theta_{1\times1}(t,\cdot)$. (b), (c) $\theta_{1\times1}$, diagonal space-time plots. $z_{\mathrm{scal}}=0.2,0.8$ in all greyscale plots.

In Fig. 6 we use $T=420$ K and the same initial conditions as in Fig. 3, but now $\vec{E}=(30,22,15,18)$kJ mol$^{-1}$. The initial evolution looks roughly the same as for the original values $\vec{E}=(28,24,15,18)$kJ mol$^{-1}$. However, for instance at $t=410$ s in (a) we see that now the top left corner itself starts to split into annular clusters, similar to a target pattern. Likewise, in the remaining part of the domain a banded structure

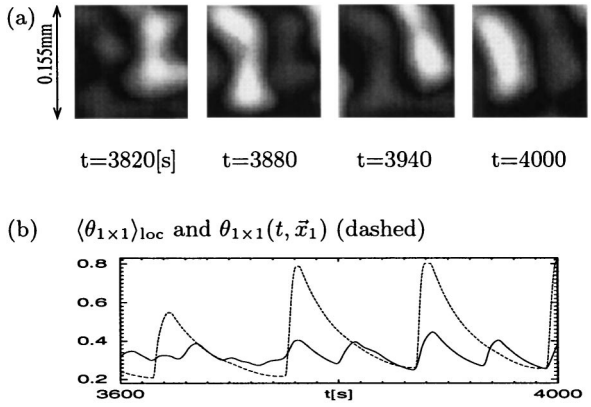


FIG. 7. Local clusters: (a) $\theta_{1\times1}(t,\cdot)$, magnification of the square of side length $L=0.155$ mm ($n=32$) in the top left corner of the simulation from Fig. 6 at large time, $z_{\mathrm{scal}}=0.2,0.8$. (b) Time series, where $\rangle\theta_{1\times1}\rangle_{\mathrm{loc}}$ denotes the spatial average over the small square.

appears where the bands of equal phase have a width of approximately 0.05–0.08 mm. Hence the clusters now have an intrinsic spatial scale. Therefore this solution is called a standing wave. This initial evolution can be nicely traced in the space-time plot (b).

However, the circular SW is not stable. Therefore, triggered by unavoidable numerical errors, for $t>1000$ s the solution gradually loses its symmetry and standing waves appear in an irregular way [third row in (a)]. This continues for large time and leads to the irregular space-time plot (c) and to irregular small amplitude oscillations of $\langle\theta_{1\times1}\rangle$ (d).

In Fig. 7 we illustrate that locally this irregular regime still shows antiphase clustering. The snapshots in (a) are blow-ups of the solution from Fig. 6 at large time in the square of side length 0.155 mm in the top left corner, showing antiphase oscillations of clusters with a spatial scale of about 0.05 mm–0.08 m, while the full line in (b) shows the local average $\langle\theta_{1\times1}\rangle_{\mathrm{loc}}$ over this part of the domain. We discuss the local dynamics of this solution again in more detail in Sec. III F.

For the present parameters, i.e., $T=420$ K, $\vec{E}=(30,22,15,18)$kJ mol$^{-1}$, and $L=0.635$ mm, random initial data as in Fig. 4 directly lead to irregular SW [34]. In 1D, irregular SW do not exist (for the present parameters) and the solution always evolves into a perfectly regular SW, also for random initial conditions. Hence, the instability of the circular SW in Fig. 6 must be attributed to curvature effects. There is, however, a strong dependence of the solution on the 2D domain size, see Fig. 9 in Sec. III E: on smaller domains the irregular SW may relax to (regular) quasi-1D SW. On the other hand, on larger domains, larger circular SW (more annuli) may develop from localized initial data before becoming unstable. This suggests that the instability of the circular SW comes from the collision of the SW with itself due to the periodic boundary conditions.

### D. Temperature dependence

In Fig. 8 we use the irregular solution at $t=2000$ s from Fig. 6 ($T=420$ K) as initial condition at lower $T$ while keep-

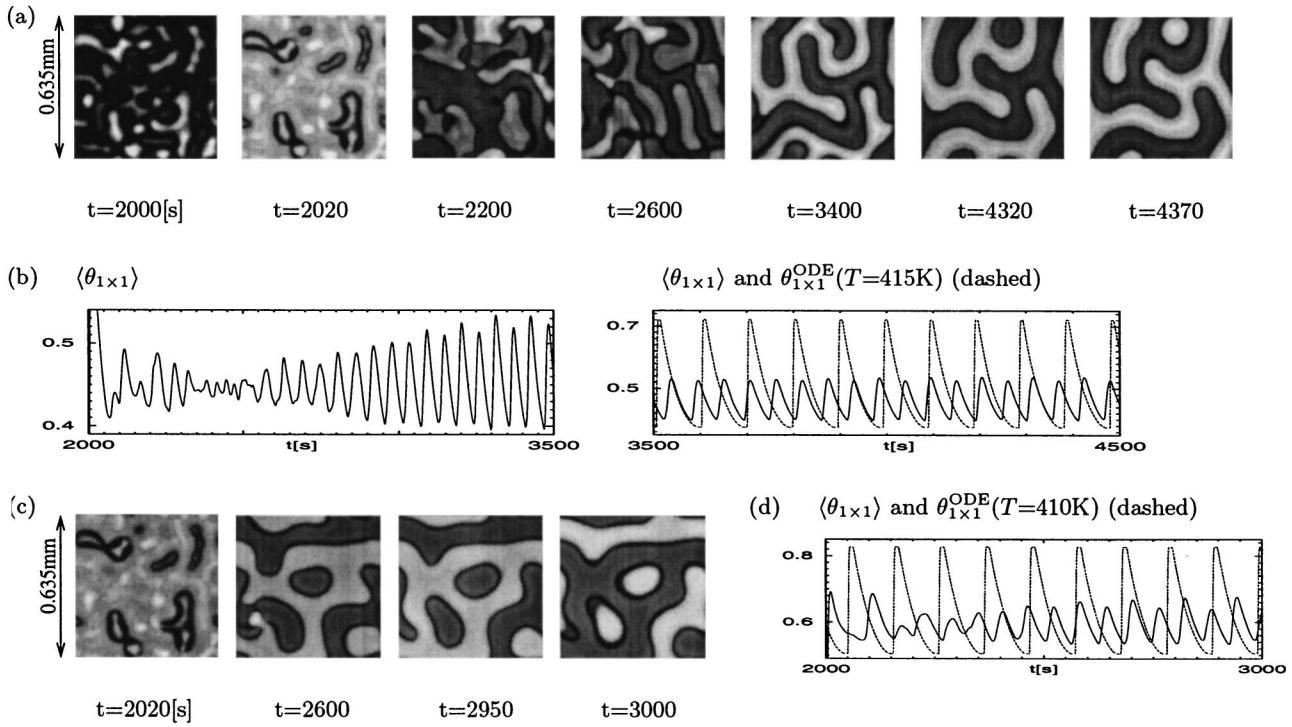


FIG. 8. Temperature dependence: $\vec{E}=(30,22,15,18)\mathrm{kJ\,mol^{-1}}$, $L=0.635$ mm, initial data from $t=2000$ in Fig. 6; $T=415$ K in (a), (b), $T=410$ K in (c), (d). (a) $\theta_{1\times1}(t,\cdot)$, $z_{\mathrm{scal}}=0.3,0.8$. (b) $\langle\theta_{1\times1}\rangle$ during transient and for nearly periodic solution, together with $\theta_{1\times1}^{\mathrm{ODE}}(T=415\ \mathrm{K})$ (dashed). (c) $\theta_{1\times1}(t,\cdot)$, $z_{\mathrm{scal}}=0.4,0.9$. (d) $\langle\theta_{1\times1}\rangle$ for (c) and $\theta_{1\times1}^{\mathrm{ODE}}(T=410\ \mathrm{K})$. Lowering temperature leads to regular SW with a larger spatial scale. The local dynamics of the solution in (a) near $t=2600$ s will also be discussed in Sec. III F.

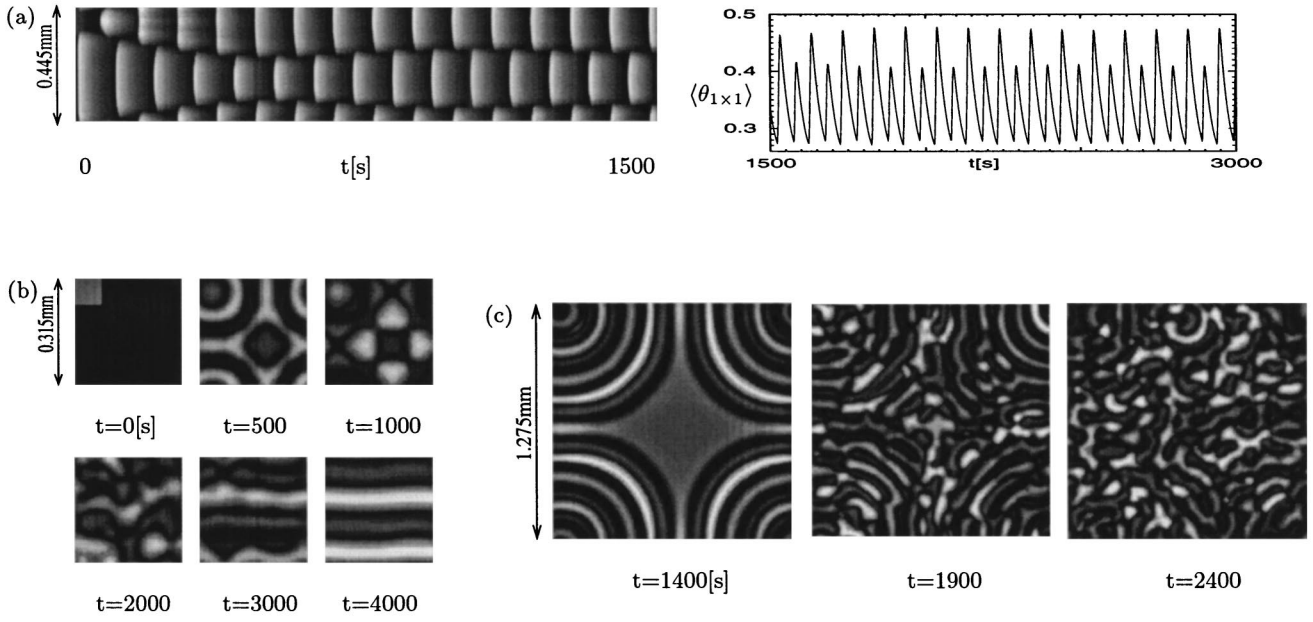


FIG. 9. Dependence on system size, $T=420$ K in all simulations: (a) $\vec{E}=(28,24,15,18)\mathrm{kJ\,mol^{-1}}$, $L=0.315$ mm, diagonal plot of $\theta_{1\times1}$, and time series $\langle\theta_{1\times1}\rangle(t)$. (b) $\vec{E}=(30,22,15,18)\mathrm{kJ\,mol^{-1}}$, $L=0.315$ mm ($n=64$), $\theta_{1\times1}(t,\cdot)$. (c) $\vec{E}=(28,24,15,18)\mathrm{kJ\,mol^{-1}}$, $L=1.275$ mm ($n=256$), $\theta_{1\times1}(t,\cdot)$. (a) corresponds to the simulation from Fig. 3 (PC) on a four times smaller domain, (b)/(c) correspond to the simulation from Fig. 6 on a four times smaller/larger domain.

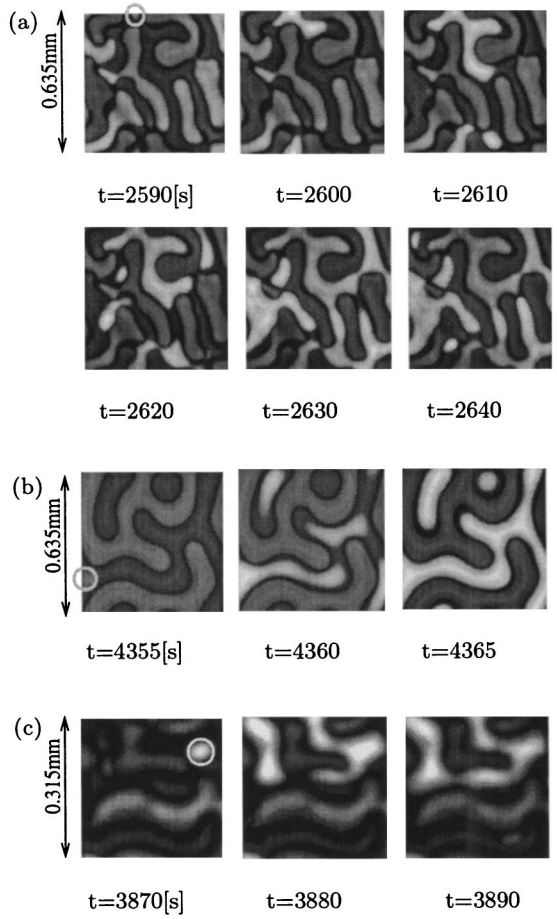


FIG. 10. Nucleation and local fronts within clusters: (a) and (b) show again $\theta_{1\times1}(t,\cdot)$ for the solution from Fig. 8(a). (c) shows $\theta_{1\times1}$ in the top left quarter of the solution from Fig. 6, see also Fig. 7. In the first frames the location of cluster nuclei have been marked by circles. From (a) and (c) we may estimate local front speeds $c \approx 1.25\times10^{-3}$ cm s$^{-1}$ and $c\approx10^{-3}$ cm s$^{-1}$, respectively.

ing the remaining parameters $\vec{E}=(30,22,15,18)$kJ mol$^{-1}$ fixed. In other words, at $t=2000$ s we instantaneously lower temperature. The snapshots in (a) ($T=415$ K) show that this yields a rearrangement of the phase clusters on a larger spatial scale. For $t>3400$ s the solution is nearly periodic: the cluster boundaries drift only slightly between the fifth frame ($t=3400$ s) and the sixth frame ($t=4320$ s) in (a). The second time series in (b) shows that the period and amplitude of $\langle\theta_{1\times1}\rangle$ are reduced by a factor of roughly $1/2$ compared to $\theta_{1\times1}^{\mathrm{ODE}}$. More accurately, the, quotient of the periods is $4/7$ which shows that the clustering also introduces a small time lag for each oscillator. In (c), (d) we use the same initial conditions and set $T=410$ K. Here, compared to (a, b) the solution becomes nearly periodic after a shorter transient and with a larger spatial scale for the clusters.

These two simulations illustrate the general temperature dependence of the model which is as in the 1D case and can be summarized as follows: at lower temperatures, BO and PW dominate over PC and SW. For instance, using the initial data and remaining parameters from Fig. 3 at $T=415$ K we get BO. Conversely, at higher temperatures clustering dominates over BO and PW. In the clustering regime, the spatial scale of SW decreases (increases) with increasing (decreasing) temperature. As discussed in Sec. IV the temperature dependence of the experiment is reverse.

Lowering temperature has two effects: it makes the periodic ODE orbits less anharmonic, and it decreases diffusion. To avoid the second effect we for instance reran the simulation from Fig. 3 at $T=415$ K but with the diffusion constants from $T=420$ K. This again gives BO. Hence, the *second key ingredient for the clustering* is the relaxation type of the ODE oscillations, which becomes sharper at larger $T$. We remark that the numerics also become more difficult at larger $T$ and the model may fail due to violation of certain mass balances; see Ref. [9] for more details (in the 1D case).

### E. Dependence on system size

In 2D, the dependence on system size is much stronger than in 1D. This is illustrated in Fig. 9. In (a) we again use the parameters from Fig. 3 but with $L=0.315$ mm ($n=64$). This again yields a PC but now with only small oscillations of the cluster boundaries, i.e., the solution becomes almost perfectly periodic.

Panels (b) and (c) show the solution with the parameters from Fig. 6 on a smaller and on a larger domain. For $n=64$ in (b) the circular SW in the top left corner breaks up around $t=800$ s and gradually more irregular SW appear. However, compared to Fig. 6, for a large time a regime sets in on the smaller domain. Near $t=2400$ s horizontal bands of equal phase become dominant. These get slowly smoothed out and adjust their spacing, and the solution relaxes to a horizontal SW in a long transient process. No such relaxation was observed on the larger domain in Fig. 6 during simulation time, see in particular Fig. 6(e) and 6(f), and we do not expect it to happen for even larger times. Of course, quasi-1D SW are asymptotically stable independent of the domain size, but the irregular SW in Fig. 6 does not seem to be in the domain of attraction of such a quasi-1D SW.

Conversely, using the same parameters on a domain four times larger than in Fig. 6, the circular SW becomes larger and survives longer. The remnants can still be identified at $t=1900$ s in (c). Hence, the instability may be due to the collision of the circular SW with itself, or, more generally, from the interaction of convex and concave regions. The time- series of $\langle\theta_{1\times1}\rangle$ for the solution in (b) is similar to Fig. 6(f), but the oscillations become even more irregular. This simulation (up to $t=2400$ s) took 12 days on a 2.4 GHz Pentium 4 machine with 512 MB RAM.

Hence, the system size must be chosen with care; for the parameters considered here $L=0.635$ mm ($n=128$) seems to capture the relevant phenomena in acceptable computation time.

### F. Local fronts within clustered solutions

For PC and SW (at least away from irregular regimes), the time series for $\langle\theta_{1\times1}\rangle$ and similar averaged quantities shows 2 maxima during (roughly) one ODE-oscillation period, while $\langle\theta_{1\times1}\rangle$ in SW has the same period as $\theta_{1\times1}^{\mathrm{ODE}}$. Moreover,

TABLE II. Rate constants for the NO+NH3 reactions on Pt(100).

| Reaction step | Param. | $\nu_i$ ($s^{-1}$) | $E_i$ (kcal$\times$mol$^{-1}$) | Value at 420 K ($s^{-1}$) |
|---|---|---|---|---|
| NO desorption $1\times1$ | $k_1$ | $1.7\times10^{14}$ | 37.0[a] | $9.7\times10^{-6}$ |
| NO dissociation $1\times1$ | $k_2$ | $2.0\times10^{15}$ | 28.5 | 3.0 |
| NO trapping on $1\times1$ | $k_3$ | $2.2\times10^{4}$ | 8.0 | 1.52 |
| NO desorption hex | $k_4$ | $4.0\times10^{12}$ | 26.0 | 0.12 |
| $NH_3$ desorption $1\times1$ | $k_5$ | $1.0\times10^{9}$ | 18.0[a] | 0.43 |
| $NH_3$ dissociation $1\times1$ | $k_6$ | $1.0\times10^{15}$ | 27.5 | 4.98 |
| $NH_3$ formation $1\times1$ | $k_7$ | $1.0\times10^{10}$ | 16.0 | 47.7 |
| $H_2O$ formation $1\times1$ | $k_8$ | $1.0\times10^{13}$ | 13.0 | $1.73\times10^{6}$ |
| $N_2$ desorption $1\times1$ | $k_9$ | $1.3\times10^{12}$ | 19.0 | $1.70\times10^{2}$ |
| $H_2$ desorption $1\times1$ | $k_{10}$ | $8.0\times10^{12}$ | 23.0 | 8.72 |
| Transition $1\times1\rightarrow$hex | $k_{11}$ | $2.5\times10^{11}$ | 25.0 | $2.48\times10^{-2}$ |

[a]For zero local coverage, see Eq. (A2).

unlike PC and SW, PW may be describable by pure phase models. This is why so far we made a clear distinction between clustered solutions (PC and SW) and PW.

Now we show that the distinction is more gradual, which is important for the comparison of the numerical results with experimental data in Sec. IV. Strictly speaking, "cluster of equal phase" means that the cluster appears "all at once" in the greyscale plots used here. This is not the case. Instead, using smaller time intervals between the frames for the greyscale plots, we now point out that there are *cluster nuclei* from which the cluster appear via *local front dynamics*. In fact, this can already be seen in 1D since the front sides of the clusters are not straight lines but bended [e.g., Figs. 2(b) and 2(c)]. Now we want to give more quantitative statements.

In Fig. 10(a) we return to the fourth frame in Fig. 8. Note that this is in a transient regime. However, this is similar to the experimental situation since there it is difficult to maintain constant conditions for the system over long times: typically the partial pressures slowly drift in the experiments, for instance due to adsorption at the chamber walls. Moreover, in experiments often temperature ramps are used. In the first frame in (a) ($t=2590$ s) a cluster nucleus has been marked by a grey circle. From here a cluster grows which at $t=2620$ s has reached roughly the center of the domain by a local front. The distance between the nucleus at $t=2590$ s and the front position at $t=2620$ s is about $75\times0.005$ mm. From this we may estimate a front speed $c\approx1.25\times10^{-3}$ cm s$^{-1}$. Similar cluster nuclei and local front dynamics can be identified in the other frames in (a). These give rather larger estimates for the local front speeds.

In (b) we illustrate the same mechanism in the fully developed clustering regime. Now the time difference between the appearance of the cluster nucleus ($t=4355$ s) and the full appearance of the cluster ($t=4365$ s) is much smaller. Here the estimate of a local front makes less sense. For the irregular solution from Fig. 6 the local front dynamics can be seen for all time. From (c) we estimate $c\approx(20\times0.005\text{ mm})/(10\text{ s})=10^{-3}$ cm s$^{-1}$ for the local front speed.

## IV. DISCUSSION AND CONCLUSIONS

The dependence of the model (2) on the diffusion energies and temperature can be summarized as follows:

(a) For the diffusion energies in Table I we obtain PC solutions, provided the initial perturbations of a homogenous surface near the periodic ODE orbit are large enough.

(b) Decreasing diffusion of $\theta_{NO}^{1\times1}$ and/or increasing diffusion of $\theta_{NO}^{hex}$ first introduces and then decreases a spatial length scale for the clusters, i.e., it shifts the system to the SW regime.

(c) One key ingredient of both PC and SW is the relatively fast diffusion of $\theta_{NH_3}^{1\times1}$ and $\theta_{H}^{1\times1}$. For slower diffusion of $\theta_{NH_3}^{1\times1}$, $\theta_{H}^{1\times1}$ no clustering appears but phase waves. This is in contrast to CO+$O_2$ on Pt(110) [10–13,23–26] where clustering has only been reported under a global coupling through the gas phase. This global coupling is replaced here by the fast diffusion of $\theta_{NH_3}^{1\times1}$, $\theta_{H}^{1\times1}$.

(d) Temperature dependence: at lower temperatures, BO and PW dominate over PC and SW, while at higher temperatures clustering dominates over BO and PW. In the clustering regime, the spatial scale of SW increases (decreases) with decreasing (increasing) temperature.

These overall features have been confirmed in a number of further simulations not presented here; see also Ref. [34]. They are as in 1D [9]. The *new feature in 2D* are curvature effects. In particular, these can lead to large amplitude oscillations of the cluster boundaries (Fig. 3), to a failure of phase balancing [Figs. 8 and 9(a)], and, on sufficiently large domains, to irregular standing waves [Figs. 6 and 9(c)].

Mathematical explanations for the observed solutions are difficult even for the basic phenomena in 1D, like the clustering as such and the different roles of the diffusion constants. In particular, it is unclear if the 1D problem can be

TABLE III. Temperature independent parameters.

| Description | Param. | Value |
|---|---|---|
| NO-adsorption flux $1\times1$, hex | $F_{NO}$ | $2.21\times10^5(\text{mbar}^{-1}\,\text{s}^{-1})$ |
| $NH_3$-adsorption flux $1\times1$ | $F_{NH_3}$ | $2.84\times10^5(\text{mbar}^{-1}\,\text{s}^{-1})$ |
| $H_2$-adsorption flux $1\times1$ | $F_{H_2}$ | $8.28\times10^5(\text{mbar}^{-1}\,\text{s}^{-1})$ |
| Inhibition coverage of NO for NO dissociation | $\theta_{NO}^{inh}$ | 0.61 |
| Inhibition coverage of O for NO dissociation | $\theta_{O}^{inh}$ | 0.399 |
| Critical coverage of NO for the $1\times1\rightarrow$hex phase transf. | $\theta_{NO}^{crit}$ | 0.3 |
| Critical coverage of NO for the $1\times1\rightarrow$hex phase transf. | $\theta_{O}^{crit}$ | 0.4 |
| Coverage for island growth in the hex$\rightarrow1\times1$ phase transf. | $\theta_{grow}^{1\times1}$ | 0.5 |
| Amount of surface defects | $\theta_{def}$ | $1.0\times10^{-4}$ |
| Partial pressures (tunable, but kept fixed here) | $p_{NO}$ | $1.1\times10^{-6}$ mbar |
| | $p_{NH_3}$ | $4.7\times10^{-6}$ mbar |

analyzed using amplitude equations for a wave bifurcation [20–22,39], since here we are far away from a bifurcation point with harmonic time dependence of the bifurcating solutions. In 2D these problems become worse, and at present we have no explanation what causes, for instance, the oscillations of the cluster boundaries or the instability of the circular standing wave.

On the other hand, it remains to relate the results for the model (2) to the experimental results reported in Refs. [7,6]. Clustering makes the oscillations of averaged quantities more harmonic compared to the ODE oscillations and also reduces the period and amplitude by a factor of roughly 2. As a result, the time series for the averaged quantities from the simulation agree better with experimental data; for instance, the period in the ODE oscillations is too large by a factor of roughly 2 compared to experiment (Ref. [7], Fig. 7) which always includes some averaging.

The PEEM images in Ref. [6] show snapshots of various types of patterns obtained at different experimental conditions. The PEEM signal measures the difference in local work function which is a function of all the adsorbed species, where roughly black correspond to $NO_{ad}$ and $O_{ad}$, white to $NH_3$, and gray to the hex phase of the surface, i.e., to large $1-\theta_{1\times1}$. Here we chose $\theta_{1\times1}$ as diagnostic, but since the remaining variables can then roughly be read from the ODE orbit a comparison can be made.

The patterns shown in Ref. [6] have distinctive spatial scales which are on the order of $10^{-2}$ cm down to $10^{-3}$ cm. In some situations, different patterns (such as spiral waves and target patterns) on different spatial scales coexist. Irregular patterns on small spatial scales are also observed. In these, the overall reaction rates become almost stationary, while local averages still show (irregular) oscillations ([6], Figs. 5 and 6). Proper phase clustering with the splitting of the specimen into only two clusters as in Sec. III A was not observed in Ref. [6]. This might be due to the fact that rather few parameter ranges were studied with spatially resolved methods. Moreover, any real surface contains macroscopic defects like scratches that may destroy large patterns. In any case, from the available data we conclude that the estimates in Table I for the diffusion energies do not reproduce the experimental results. Instead, the diffusion energies $\vec{E}=(30,22,15,18)$ used in Figs. 6–8 yield a better agreement with experiment, though the temperature dependence of the model is still wrong, see later.

In Ref. [6], Fig. 2 a sequence of PEEM images is used to explain via front dynamics the formation of "adsorbate islands," which correspond to phase clusters in our terminology. This agrees qualitatively with the local front dynamics in Sec. III F, but the front speeds ($0.5\times10^{-4}$ cm/s and $1.1\times10^{-4}$ cm/s for two different types of fronts in the experiment) are one order of magnitude lower than in Fig. 10. Of course, we can decrease the front speed in the simulations by a factor $\alpha=1/10$ by simply changing the spatial scale, i.e., multiplying all diffusion constants uniformly by $\alpha^2$. However, this would yield some trade-off between the correct spatial scale for the patterns and the front speed.

Finally, the temperature dependences of the model (2) and of the experiment are reversed. In the latter, irregular small scale patterns are observed at the lower end of the temperature window $[T_{min},T_{max}]$ for kinetic oscillations, while for intermediate temperatures larger scale regular spatial structures dominate, and bulk oscillations near $T_{max}$. In the model (2) it is the other way round. However, the bulk oscillations at high $T$ and the gradual failure of long range synchronization at lower $T$ in the experiment are attributed to the global gas-phase coupling and its breakdown at lower $T$. As already said, such a global gas-phase coupling is not included in (2), and it remains to be seen if some of the shortcomings of (2) can resolved by including it.

## ACKNOWLEDGMENTS

The author thanks R. Imbihl and A. S. Mikhailov for stimulating discussions.

## APPENDIX: THE ODE

To make the paper somewhat self contained, we give the ODE (1) (see Refs. [7,8] for the chemical meanings and discussion);

$$\frac{d}{dt}\theta_{\mathrm{NO}}^{1\times1} = F_{\mathrm{NO}}p_{\mathrm{NO}}(\theta_{1\times1} - \theta_{\mathrm{NO}}^{1\times1} - 4\theta_{\mathrm{NH_3}}^{1\times1}) - k_1\theta_{\mathrm{NO}}^{1\times1} - k_2\frac{\theta_{\mathrm{NO}}^{1\times1}\theta_{\mathrm{empty}}^{1\times1}}{\theta_{1\times1}} + k_3\theta_{\mathrm{NO}}^{\mathrm{hex}}\theta_{1\times1}, \tag{A1a}$$

$$\frac{d}{dt}\theta_{\mathrm{NO}}^{\mathrm{hex}} = F_{\mathrm{NO}}p_{\mathrm{NO}}(\theta_{\mathrm{hex}} - \theta_{\mathrm{NO}}^{\mathrm{hex}}) - k_3\theta_{\mathrm{NO}}^{\mathrm{hex}}\theta_{1\times1} - k_4\theta_{\mathrm{NO}}^{\mathrm{hex}}, \tag{A1b}$$

$$\frac{d}{dt}\theta_{1\times1} = \begin{cases} \left(\frac{d}{dt}\theta_{\mathrm{NO}}^{1\times1}\right)/\theta_{\mathrm{grow}}^{1\times1} & \text{if } \frac{d}{dt}\theta_{\mathrm{NO}}^{1\times1} > 0 \text{ and } \theta_{\mathrm{NO}}^{1\times1} \geqslant \theta_{\mathrm{grow}}^{1\times1}\theta_{1\times1} \text{ and } \theta_{1\times1} < 1, \\ -k_{11}(\theta_{1\times1} - \theta_{\mathrm{def}}^{\mathrm{hex}})(1-c) & \text{if } \theta_{1\times1} > \theta_{\mathrm{def}}^{\mathrm{hex}} \text{ and } c < 1, \\ 0 & \text{otherwise,} \end{cases} \tag{A1c}$$

$$\frac{d}{dt}\theta_{\mathrm{NH_3}}^{1\times1} = F_{\mathrm{NH_3}}p_{\mathrm{NH_3}}(\theta_{1\times1} - 3\theta_{\mathrm{NH_3}}^{1\times1} - 1.6\theta_{\mathrm{NO}}^{1\times1}) - k_5\theta_{\mathrm{NH_3}}^{1\times1} - k_6\frac{\theta_{\mathrm{NH_3}}^{1\times1}[\theta_{1\times1} - \theta_{\mathrm{H}}^{1\times1} - 2.5(\theta_{\mathrm{O}}^{1\times1} + \theta_{\mathrm{N}}^{1\times1})]}{\theta_{1\times1}} + k_7\frac{\theta_{\mathrm{N}}^{1\times1}\theta_{\mathrm{H}}^{1\times1}}{\theta_{1\times1}}, \tag{A1d}$$

$$\frac{d}{dt}\theta_{\mathrm{O}}^{1\times1} = k_2\frac{\theta_{\mathrm{NO}}^{1\times1}\theta_{\mathrm{empty}}^{1\times1}}{\theta_{1\times1}} - k_8\frac{\theta_{\mathrm{O}}^{1\times1}\theta_{\mathrm{N}}^{1\times1}}{\theta_{1\times1}}, \tag{A1e}$$

$$\frac{d}{dt}\theta_{\mathrm{N}}^{1\times1} = k_2\frac{\theta_{\mathrm{NO}}^{1\times1}\theta_{\mathrm{empty}}^{1\times1}}{\theta_{1\times1}} + k_6\frac{\theta_{\mathrm{NH_3}}^{1\times1}[\theta_{1\times1} - \theta_{\mathrm{H}}^{1\times1} - 2.5(\theta_{\mathrm{O}}^{1\times1} + \theta_{\mathrm{N}}^{1\times1})]}{\theta_{1\times1}} - k_7\frac{\theta_{\mathrm{N}}^{1\times1}\theta_{\mathrm{H}}^{1\times1}}{\theta_{1\times1}} - k_9\frac{(\theta_{\mathrm{N}}^{1\times1})^2}{\theta_{1\times1}}, \tag{A1f}$$

$$\frac{d}{dt}\theta_{H}^{1\times1} = F_{\mathrm{H_2}}p_{\mathrm{H_2}}\frac{[\theta_{1\times1} - \theta_{\mathrm{H}}^{1\times1} - 2.5(\theta_{\mathrm{O}}^{1\times1} + \theta_{\mathrm{N}}^{1\times1})]^2}{\theta_{1\times1}} + 3k_6\frac{\theta_{\mathrm{NH_3}}^{1\times1}[\theta_{1\times1} - \theta_{\mathrm{H}}^{1\times1} - 2.5(\theta_{\mathrm{O}}^{1\times1} + \theta_{\mathrm{N}}^{1\times1})]}{\theta_{1\times1}} - 3k_7\frac{\theta_{\mathrm{N}}^{1\times1}\theta_{\mathrm{H}}^{1\times1}}{\theta_{1\times1}} - 2k_8\frac{\theta_{\mathrm{O}}^{1\times1}\theta_{\mathrm{H}}^{1\times1}}{\theta_{1\times1}} - k_{10}\frac{(\theta_{\mathrm{H}}^{1\times1})^2}{\theta_{1\times1}}. \tag{A1g}$$

The three conditions on the right hand side of (A1c) have to be read top down and the first one fulfilled determines the right hand side. The rate constants $k_1, \ldots, k_{11}$ are determined by Arrhenius-law $k_i = \nu_i e^{-E_i/RT}$, where the $\nu_i$ and most of the $E_i$ are constants, given in Table II. For $E_1$ and $E_5$ coverage-dependent nonlinear corrections are used in the form

$$E_1 = E_1^0 - 24(\theta_{\mathrm{NO}}^{1\times1}/\theta_{1\times1})^2, \quad E_5 = E_5^0 - 30(\theta_{\mathrm{NH_3}}^{1\times1}/\theta_{1\times1})^2. \tag{A2}$$

The auxiliary functions in (A1) are given by

$$\theta_{\mathrm{empty}}^{1\times1} = \max\left[\left(\theta_{1\times1} - \frac{\theta_{\mathrm{NO}}^{1\times1}}{\theta_{\mathrm{NO}}^{\mathrm{inh}}} - \frac{\theta_{\mathrm{O}}^{1\times1}}{\theta_{\mathrm{O}}^{\mathrm{inh}}}\right), 0\right] + \max[(\theta_{\mathrm{def}}^{1\times1} - \theta_{\mathrm{O}}^{1\times1}), 0],$$

$$c = \left(\frac{\theta_{\mathrm{NO}}^{1\times1}}{\theta_{\mathrm{NO}}^{\mathrm{crit}}} + \frac{\theta_{\mathrm{O}}^{1\times1}}{\theta_{\mathrm{O}}^{\mathrm{crit}}}\right) \Big/ \theta_{1\times1}, \quad \theta_{1\times1} + \theta_{\mathrm{hex}} = 1,$$

$$\theta_{\mathrm{def}}^{1\times1} = \theta_{1\times1}\theta_{\mathrm{def}}, \quad \theta_{\mathrm{def}}^{\mathrm{hex}} = \theta_{\mathrm{hex}}\theta_{\mathrm{def}},$$

and the further parameters are given in Table III.


[1] M. Eiswirth and G. Ertl, in *Chemical Waves and Patterns*, edited by R. Kapral and K. Showalter (Kluwer, Dordrecht, 1995), pp. 447–483.

[2] G. Ertl, Adv. Catal. **37**, 213 (1990).

[3] R. Imbihl, Prog. Surf. Sci. **44**, 185 (1993).

[4] R. Imbihl and G. Ertl, Chem. Rev. (Washington, D.C.) **95**, 697 (1995).

[5] S. J. Lombardo, F. Esch, and R. Imbihl, Surf. Sci. **271**, L367 (1992).

[6] G. Veser, F. Esch, and R. Imbihl, Catal. Lett. **13**, 371 (1992).

[7] S. J. Lombardo, T. Fink, and R. Imbihl, J. Chem. Phys. **98**, 5526 (1993).
[8] H. Uecker, R. Imbihl, M. Rafti, I. M. Iruzun, J. L. Vicente, and E. E. Mola, Chem. Phys. Lett. **382**, 232 (2003).
[9] H. Uecker, Physica D **190**, 249 (2004).
[10] M. Bär, M. Hildebrand, M. Eiswirth, M. Falcke, H. Engel, and M. Neufeld, Chaos **4**, 499 (1994).
[11] M. Bertram and A. S. Mikhailov, Phys. Rev. E **63**, 066102 (2001).
[12] M. Falcke, H. Engel, and M. Neufeld, Phys. Rev. E **52**, 763 (1995).
[13] A. v. Oertzen, H. H. Rotermund, A. S. Mikhailov, and G. Ertl, J. Phys. Chem. B **104**, 3155 (2000).
[14] Y. Kuramoto, *Chemical Oscillations, Waves, and Turbulence*, *Springer Series in Synergetics*, Vol. 19 (Springer-Verlag, Berlin 1984).
[15] A. S. Mikhailov, *Foundations of Synergetics I. Distributed Active Systems* (Springer-Verlag, Berlin, 1990).
[16] D. Walgraef, *Spatio–Temporal Pattern Formation* (Springer-Verlag, New York, 1997).
[17] E. M. Izhikevich, SIAM (Soc. Ind. Appl. Math.) J. Appl. Math. **60**, 1789 (2000).
[18] V. I. Nekorkin and M. G. Velarde, *Synergetic Phenomena in Active Lattices—Patterns, Waves, Solitons, Chaos* (Springer-Verlag, Berlin, 2002).
[19] D. Somers and N. Kopell, Physica D **89**, 169 (1995).
[20] S. Krömker, Acta Math. Univ. Comen. **67**, 83 (1998).
[21] H. Levine and X. Zou, Phys. Rev. E **48**, 50 (1993).
[22] A. M. Zhabotinsky, M. Dolnik, and I. R. Epstein, J. Chem. Phys. **103**, 10306 (1995).
[23] M. Bertram, C. Beta, M. Pollmann, A. S. Mikhailov, H. H. Rotermund, and G. Ertl, Phys. Rev. E **67**, 036208 (2003).
[24] M. Bertram and A. S. Mikhailov, Phys. Rev. E **67**, 036207 (2003).
[25] M. Falcke and H. Engel, J. Chem. Phys. **101**, 6255 (1994).
[26] K. C. Rose, D. Battogtokh, A. Mikhailov, R. Imbihl, W. Engel, and A. M. Bradshaw, Phys. Rev. Lett. **76**, 3582 (1996).
[27] M. Kim, M. Bertram, M. Pollmann, A. von Oertzen, A. Mikhailov, H. H. Rotermund, and G. Ertl, Science **292**, 1357 (2001).
[28] M. Sheintuch and O. Nekhamkina, J. Chem. Phys. **107**, 8165 (1997).
[29] V. K. Vanag, L. Yang, M. Dolnik, A. M. Zhabotinsky, and I. R. Epstein, Nature (London) **406**, 389 (2000).
[30] V. K. Vanag, A. M. Zhabotinsky, and I. R. Epstein, J. Phys. Chem. A **104**, 11566 (2000).
[31] L. Yang, M. Dolnik, A. M. Zhabotinsky, and I. R. Epstein, Phys. Rev. E **62**, 6414 (2000).
[32] E. M. Nicola, M. Or-Guil, W. Wolf, and M. Bär, Phys. Rev. E **65**, 055101(R) (2002).
[33] F. Mertens, R. Imbihl, and A. Mikhailov, J. Chem. Phys. **99**, 8668 (1993).
[34] H. Uecker, www.math.uni-karlsruhe.de/~uecker/chem/
[35] J. V. Barth, Surf. Sci. Rep. **40**, 75 (2000).
[36] E. G. Seebauer and C. E. Allen, Prog. Surf. Sci. **49**, 265 (1995).
[37] Y. Kuramoto, H. Nakao, and D. Battogtokh, Physica A **288**, 244 (2000).
[38] P. Deuflhard and F. Bornemann, *Scientific Computing with Ordinary Differential Equations, Texts in Applied Mathematics*, Vol. 42 (Springer-Verlag, New York, 2002).
[39] H. Riecke and L. Kramer, Physica D **137**, 124 (2000).